SCIENTIFIC REP🗲RTS

Scalable Epitaxial Growth of WSe$_2$ Thin Films on SiO$_2$/Si *via* a Self-Assembled PtSe$_2$ Buffer Layer

Pei-Chen Wu, Chun-Liang Yang, Yuanmin Du & Chih-Huang Lai

The growth of large-area epitaxial transition metal dichalgogenides (TMDCs) are of central importance for scalable integrated device applications. Different methods have been developed to achieve large-sized high quality films. However, reliable approaches for centimeter-sized or even wafer-level epitaxial growth of TMDCs are still lacking. Here we demonstrate a new method to grow inch-sized epitaxial WSe$_2$ films on SiO$_2$/Si substrates at a much lower temperature with high repeatability and scalability. High quality crystalline films are achieved through direct selenization of a tungsten film with platinum as the underlayer. The self-assembled PtSe$_2$ buffer layer, formed during selenization, assists epitaxial growth of WSe$_2$. Using fabricated WSe$_2$ films, excellent performance memory devices are demonstrated. As a member of the TMDC family, our findings based on WSe$_2$ may also be applied to other TMDC materials for large-scale production of high quality TMDC films for various applications.

Owing to the strong in-plane covalent bonds and weak van der Waals bonding between adjacent layers, layered materials have been extensively studied in the past decade due to their attractive properties[1–4]. As two-dimensional inorganic analogues of graphene, transition metal dichalgogenides (TMDCs) with the formula MX$_2$, where M is a transition metal atom and X is a chalcogen atom, have shown great potential for nanoelectronic device applications such as transistors[5–8], optoelectronic devices[9–12], and energy storage devices[13,14]. With a lattice structure similar to well-known MoS$_2$, WSe$_2$ is another interesting TMDC material. Although most of the applications require TMDC thin films with large area and good quality, the large-scale production of high quality TMDC films is still challenging.

Similar to other TMDC materials, chemical vapor deposition (CVD) is a frequently used method for WSe$_2$ synthesis[15–18]. Although CVD growth of micrometer-sized 2D WSe$_2$ structures has been well developed, it typically requires high temperature process (700 to 1300 °C) and also has the limits of the substrates used for the synthesis[16–19]. Due to large surface energy and poor wettability to the insulating substrates, the formation of WSe$_2$ tends to aggregate into amorphous structures instead of highly crystalline crystals[19,20]. Large-area CVD prepared WSe$_2$ films on glass substrates at a lower temperature from reaction of WCl$_6$ and diethyl diselenide have been reported[15], but they are composed of either platelet or needle like crystalline structure with different orientations. Through a vapor transfer method[21,22], highly textured WSe$_2$ films have been fabricated on insulating substrates, however, films with high crystallinity and scalability are still lacking. Inspired by the selenization method widely used in the fabrication of Cu(In$_{1-x}$Ga$_x$)Se$_2$ (CIGS) solar cells[23,24], here we report a new method for large-area epitaxial WSe$_2$ synthesis on SiO$_2$/Si substrates. In contrast to the widely used method of synthesis *via* selenization of WO$_3$, we demonstrate a direct approach to form WSe$_2$ by selenizing W with the assistance of a Pt underlayer. In the end, a mechanism involved with the formation of a self-assembled PtSe$_2$ buffer layer has also been proposed.

Results and Discussion

Scalable epitaxial WSe$_2$ film. A schematic illustration for the growth of WSe$_2$ is shown in Fig. 1a. To synthesize WSe$_2$, an inch-sized (up to 40 × 40 mm^2) SiO$_2$/Si substrate is firstly coated with Pt 100 nm/Ta 3 nm by magnetron sputtering at room temperature. Ta works as an adhesion layer and also promotes the growth of Pt(111)[25]. A α-phase W(110) film is then sputtered on Pt (see Supplementary Fig. S1 for details), followed by a two-step selenization process in a furnace: a first step at 350 °C for the initial selenization and another step at 550 °C for the final treatment. Figure 1b (left) shows a cross-sectional scanning electron microscopy (SEM) image of the stacked film structure. The large-area highly epitaxial growth of WSe$_2$ along the [001] direction has

Department of Materials Science and Engineering, National Tsing Hua University, 30013, Hsinchu, Taiwan. Correspondence and requests for materials should be addressed to Y.D. (email: ynmin.du@gmail.com) or C.-H.L. (email: chlai@mx.nthu.edu.tw)
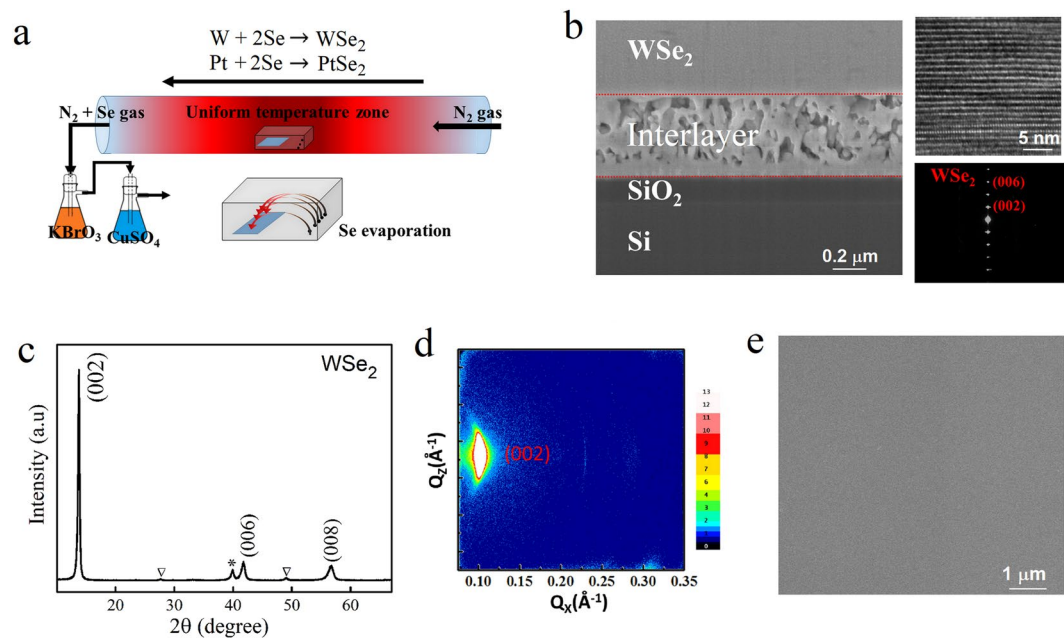
Figure 1. The epitaxial growth of WSe$_2$. (**a**) The synthesis process of WSe$_2$ with a W/Pt/Ta/SiO$_2$/Si substrate through a two-step selenization process. (**b**) Cross-sectional SEM image of a FIB-prepared lamella. Right up is a TEM image for WSe$_2$, and right below is the SAED pattern, confirming the [001] oriented WSe$_2$ lattice structure. (**c**) XRD patterns of the stacked film. Highly [001] orientated WSe$_2$ is shown. ∇ and * stand for peaks from PtSe$_2$ and Pt$_2$W, respectively. (**d**) 2D-GIXRD image. (**e**) SEM top-view image of the WSe$_2$ film showing smooth surface morphology.

been achieved, depicted by the high-resolution transmission electron microscope (HRTEM) image and selected area electron diffraction (SAED) pattern (Fig. 1b, right). In addition, an interlayer with different morphology is observed below the WSe$_2$ layer (Fig. 1b SEM image). The X-ray diffraction (XRD) patterns (Fig. 1c) reveal that peaks related to the WSe$_2$ diffraction from high order (00ℓ) planes are observed. A strong WSe$_2$ (002) peak at $2\theta = 13.7°$ indicates high crystallinity of the film. In addition to the strong WSe$_2$ peaks, weak XRD peaks of Pt$_2$W and PtSe$_2$ have also been observed. The elemental W/Se ratio in the WSe$_2$ layer is close to 0.5, confirmed by energy dispersive X-ray spectroscopy (EDX) (see Supplementary Fig. S2 for details), indicating a good stoichiometry of the synthesized WSe$_2$ film. To further reveal the in-plane crystalline property of the film, two-dimensional grazing incidence XRD (2D-GIXRD) is performed. As shown in Fig. 1d, a sharp and strong spot from WSe$_2$ (002) is observed, indicating the high quality of the epitaxial film. Figure 1e shows a top-view SEM image of the WSe$_2$ film. The fabricated WSe$_2$ films have a smooth surface, which is generally required for large–scale device fabrications.

For comparison, we also use the same process to grow WSe$_2$ directly on SiO$_2$/Si substrates, that is, direct two-step selenization of a W layer without a Pt underlayer. The XRD patterns (Fig. S3a) reveal that the intensity of WSe$_2$ (00ℓ) is much weaker for the sample without the Pt underlayer. The much poor crystalline quality for the WSe$_2$ film directly grown on SiO$_2$ is the same as the previous report[15,21]. In additon, unlike a smooth surface observed for the sample with Pt underlayer (Fig. 1e), the WSe$_2$ film without the Pt underlayer shows quite rough surface with embedded nanoflake-like structures (Fig. S3b,c), similar to the rough surface morphology reported by earlier works for large-area WSe$_2$ synthesis on dielectric substrates[15,21].

To further investigate the structure of the layered WSe$_2$ film grown by using a Pt underlayer, we perform a top-view high-angle annular dark-field scanning transmission electron microscopy (HAADF-STEM) analysis of the films obtained. Figure 2a illustrates the TEM image of a focuse ion beam (FIB) cut at the top region of the sample. It reveals a high crystalline quality of the film. Interestingly, a co-existence of 2H and 1T phases has been observed, as indicated by the enlarged images (inset of Fig. 2a). The hexagonal crystal structure of WSe$_2$ is also evaluated from the fast Fourier transformation (FFT) image in Fig. 2b,c for two selected spots. An offset of 30° between the two sets of the hexagonal spots, identified as the 2H and 1T phases respectively, has been observed, similar to the earlier reports[26–28]. In the 2H phase, the atoms are in the hexagonal symmetry with trigonal prismatic coordination, while in the 1T phase an octahedtal manner is presented. Figure 2d shows high resolution image of that shown in Fig. 2a, with the mixing of both 2H and 1T structures. The atomic resolution images further demonstrate that the tungsten and selenium atoms are arranged in a hexagonal lattice configuration of WSe$_2$, with both 2H (Fig. 2e) and 1T (Fig. 2f) structures. The high crystalline quality and co-existence of 2H and 1T are also confirmed in various regions of the sample (see Supplementary Figs S4 and S5 for more details).

X-ray photoemission spectroscopy (XPS) is conducted to acquire the binding energies of W 4f and Se 3d, as shown in Fig. 2g,h. The W 4f shows two large peaks at 34.3 eV and 32.2 eV (Group (I), color in red), attributed to the doublet W 4f$_{5/2}$ and W 4f$_{7/2}$, respectively. In addition, it also shows that there also exist two smaller peaks
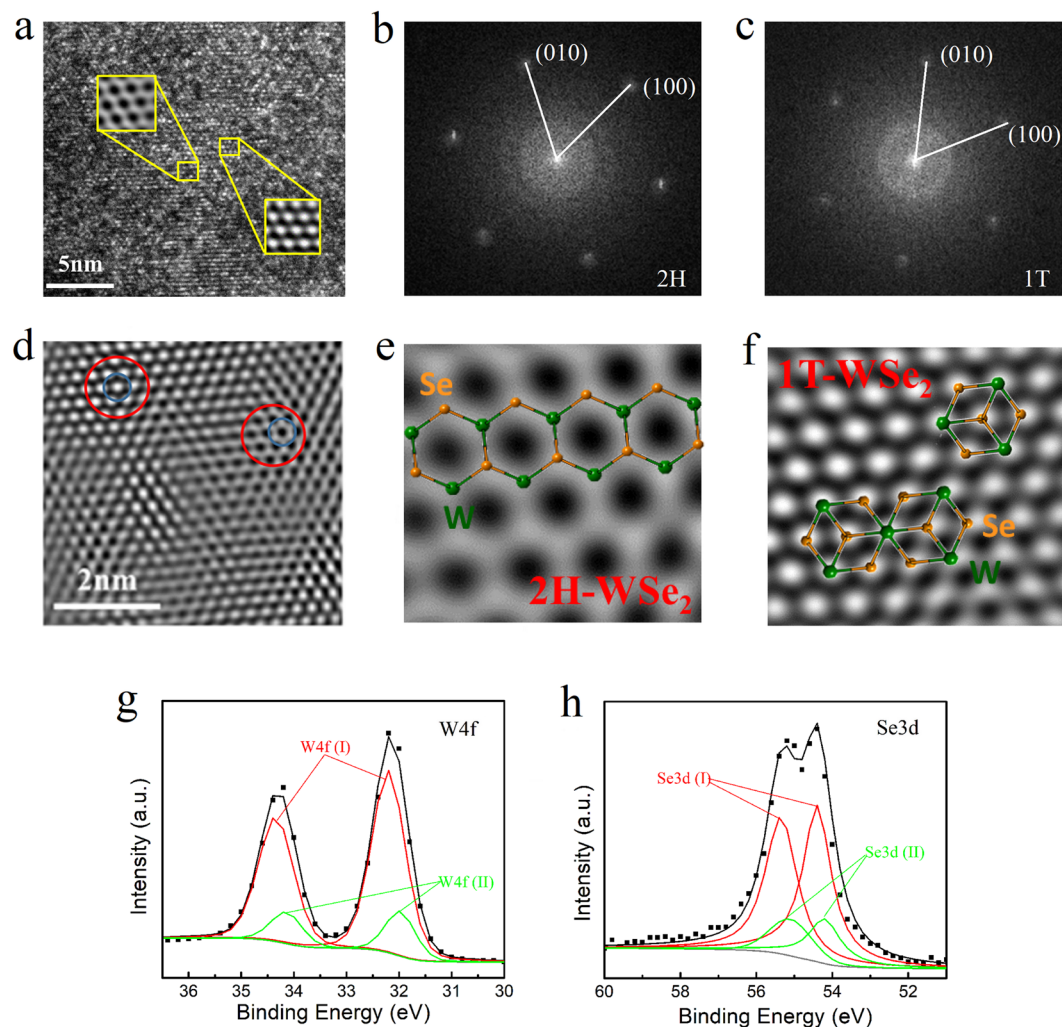
Figure 2. The co-existence of 2H and 1T WSe$_2$ structures. (**a**) Top-view TEM image after a FIB cut of the sample. Two squared regions are enlarged to show the different contrast. (**b,c**) FFT images for the 2H and 1T phases respectively, and an offset of 30° is shown. (**d**) High resolution HAADF-STEM image. (**e**) Enlarged HAADF-STEM image showing 2H hexagonal structure of WSe$_2$. (**f**) Enlarged HAADF-STEM image showing 1T hexagonal structure of WSe$_2$. (**g**) XPS spectra of W 4f and (**h**) Se 3d. Core-level peaks of WSe$_2$ from the 2H and 1T phases are shown in red and green colors, respectively.

located at 34.1 eV and 32.0 eV (Group (II), color in green), a shift of the larger peaks. According to the earlier reports[29,30], the Group (I) and Group (II) W 4f peaks can be attributed to 2H and 1T WSe$_2$ phases respectively, which further supports the coexistence of 2H and 1T forms, consistent with the TEM image analysis. Similarly, it is also observed that the doublet Se 3d peaks, corresponding to the Se 3d$_{5/2}$ and Se 3d$_{3/2}$ orbital of divalent selenium ions (Se2^-), can be separated into two groups (Fig. 2h). Compared to the semiconducting 2H phase, the 1T phase is known to be metallic and thermodynamically unstable. In our results, a stable 1T phase is consistently observed, which might come from the co-existence of its counterpart (2H phase).

We use the Raman mapping technique to explore the uniformity of the WSe$_2$ film, across the inch-sized silicon substrate, based on the two characteristic A$_{1g}$ and 2LA(M) modes[31,32] in the region from 245 to 260 cm^{-1}, as shown in Fig. 3. Figure 3a,b demonstrate the peak position mappings during the scans. Except for some outlier dots, a narrow variation of both peaks is obtained. In addition, Fig. 3c,d show the intensity mappings for the two peaks, supporting the uniform formation of epitaxial WSe$_2$ films[33,34]. Through a surface mapping, no major difference can be found on the eight points (marked as ① to ⑧ in Fig. 3f) across the sample surface, as confirmed by the Raman peak position mappings in Fig. 3e.

CVD is the frequently used method to grow 2D material films on different substrates. But the development of optimized growth of single or multiple layers in a large scale has proven to have many difficulties. In addition to CVD, one common method for obtaining TMDC monolayers is mechanical exfoliation. Although its scale-up is limited, it is expected that the mechanical exfoliation method will continue to play an important role in the development of 2D materials. While different methods[35–39] have been developed to improve the exfoliation process in the last decade, here we demonstrate the use of the original exfoliation (repeated peeling) method[35] to get good
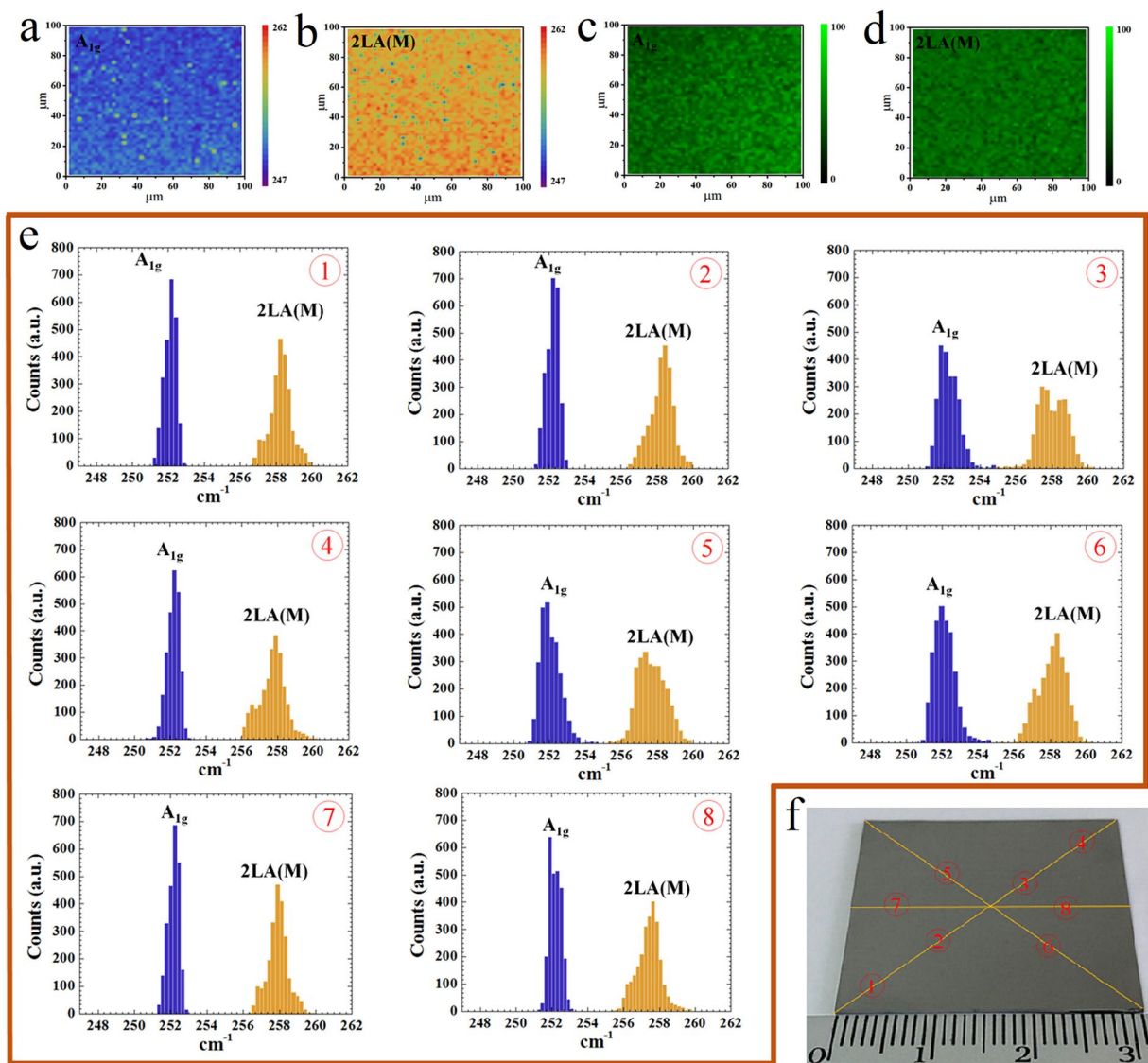
Figure 3. Characterizations of the macroscopic uniformity of the WSe$_2$ film. (**a,b**) Raman spectra mappings of a 100×100 μm^2 area of an as-deposited sample, representative to A$_{1g}$ and 2LA(M) modes respectively. (**c,d**) Corresponding Raman intensity mappings of the two Raman characteristic A$_{1g}$ and 2LA(M) modes, respectively. (**e**) Peak distributions for A$_{1g}$ and 2LA(m) modes at different positions (100×100 μm^2) on the sample surface. (**f**) Photograph of a WSe$_2$ film on SiO$_2$/Si wafer and the positions marked for Raman mappings.

quality of nanosheets from our layered WSe$_2$ films. WSe$_2$ nanosheets with different thickness after an exfoliation process are shown in Fig. 4. Figure 4a–c show the atomic force microscopy (AFM) images for the samples, with the thicknesses determined by the AFM measurements in Fig. 4d–f. Figure 4g shows the Raman spectra for WSe$_2$ with different thickness. The 2LA(M), A$_{1g}$, E(M) and E(K) are Raman modes corresponding to different scattering modes according to the report[31]. A good consistency of the Raman spectra has been shown for the exfoliated films. With the thickness going down to 15.1 nm, the A$_I$ mode starts to appear[31]. Figure 4h shows the Raman spectrum of the 3.8 nm sample (~5 monolayers), for which a strong A$_I$ mode has been shown. The appearance of the A$_I$ band could be due to an interlayer vibration mode, which is reported to exist at a few layers[31,40]. The quality of the bulk crystal, and the van der Waals forces between the sheets of the layered structure determine the exfoliation process. Figure 4i shows one example of the exfoliated WSe$_2$ flake after a liquid exfoliation process similar to the method described by Lin *et al.*[39]. The promising result achieved here means that we may get even larger areas of WSe$_2$ 2D films, by using an improved method. We also need to mention that, through Raman analysis of the exfoliated films, no PtSe$_2$ spectrum has been found, indicating high purity of the WSe$_2$ films obtained.

To demonstrate and evaluate the electrical performance of the fabricated WSe$_2$ films, stacked device structures are fabricated. Figure 5a,b show the typical current-voltage (I-V) characteristics of the device fabricated using the as grown WSe$_2$ film, with Pt as the top electrode. A remarkable I-V performance has been shown, with high repeatability and reliability. It is a kind of capacitance memory effect, according to the report by Paul *et al.*[41]. Through the application of an external electrical field, charge storage and retention can be achieved. By utilizing
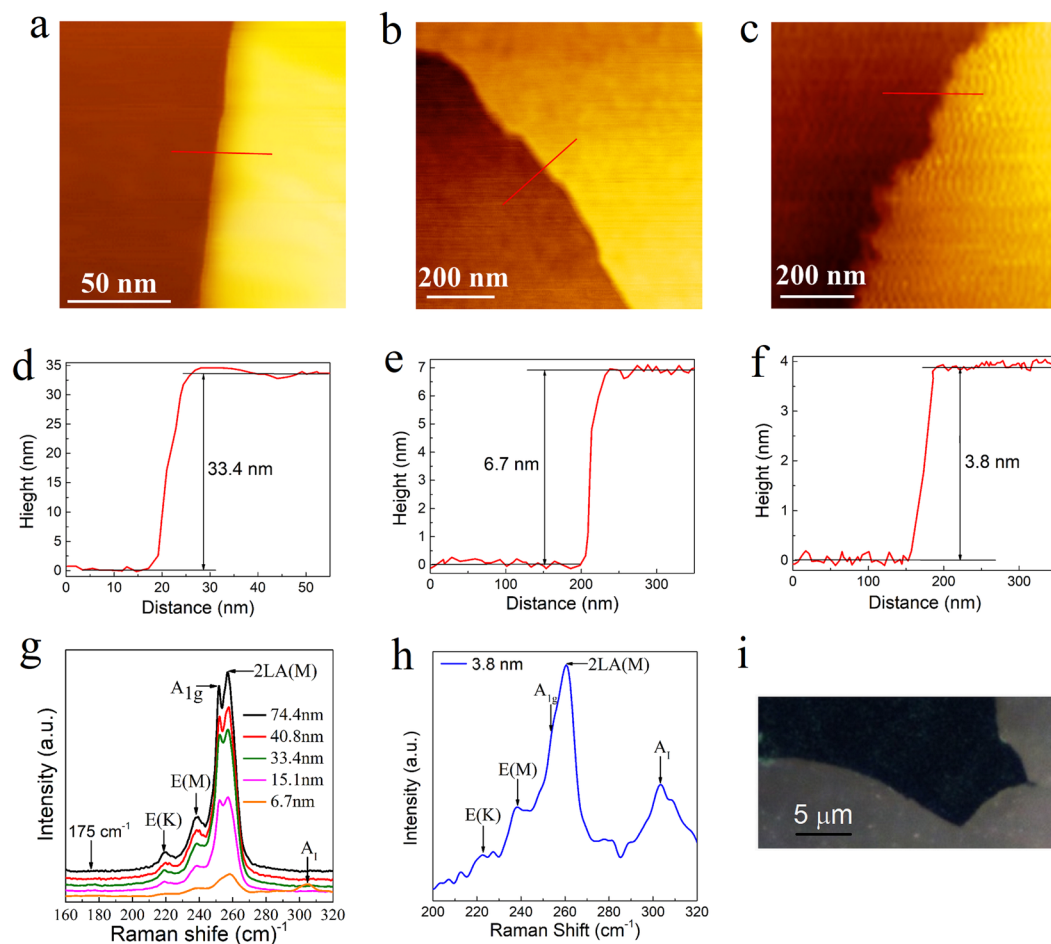
Figure 4. WSe$_2$ flakes with different thickness after an exfoliation process. (**a–c**) AFM images, and (**e,f**) the corresponding height profiles (acquired on the area highlighted with a red line) for the WSe$_2$ flakes. (**g**) Raman spectra of the exfoliated films with different thickness. 2LA(M), A$_{1g}$, E(M), E(K) and A$_I$ stand for different Raman modes for WSe$_2$. 175 cm^{-1} refers to the position of the characteristic mode (E$_g$) for PtSe$_2$, and no peak is present. (**h**) Raman spectrum of WSe$_2$ with 3.8 nm thickness. (**i**) Optical image of a WSe$_2$ flake after a liquid exfoliation process.

the 2H-1T phase transition of MoS$_2$ in a battery cell, high levels of pseudocapacitive charge storage have been reported by Cook *et al.* recently[42]. While the detailed mechanism needs to be further explored for our device structure, the highly repeatable result (more than 3000 cycles) indicates that the fabricated film has a good potential for battery material applications. Memory devices using an exfoliated WSe$_2$ nanosheet are also fabricated. Figure 5c shows a resistive random access memory (ReRAM) device, through transferring a WSe$_2$ nanosheet to a Cu bottom electrode on SiO$_2$/Si, followed by deposition of the Pt top electrode. After an electroforming process[43,44], a good resistive switching behavior has been observed (Fig. 5d). The switching from a low resistance state (LRS) to a high resistance state (HRS) occurs at a negative voltage −1.4 V, and vice versa at a positive voltage 1.7 V, with a resistance ratio at ~10^2. It is a kind of bi-polar switching behavior[44], with substantially low switching voltages, compatible with existing complementary metal-oxide-semiconductor (CMOS) integrated transistors. Such merits make it a good candidate for low power and high density device applications.

Mechanism. The above results are based on the analysis of a sample with Pt and W both at 100 nm before the selenization process, from which a WSe$_2$ film ~365 nm is finally obtained. Through tuning the W and Pt thicknesses, good crystallinity WSe$_2$ films with different thicknesses from a few nanometers to the micrometer range have also been fabricated (see Supplementary Figs S6 and S7 for more details). We also verify the thickness relationship between the as-deposited W film and selenized WSe$_2$ films (Fig. S7d). In this section, we will discuss the underlying mechanism involved in the epitaxial growth process of WSe$_2$.

Figure 6 shows the XRD patterns of the samples by changing the growth conditions. Sample I is grown at the selenization temperature of 350 °C, and neither WSe$_2$ or PtSe$_2$ peaks are shown. Sample II is firstly heated at 350 °C, then increased to 450 °C. At this condition, WSe$_x$ (x < 2) starts to appear but the growth rate is very slow. Sample III is firstly heated at 350 °C and then increased to 550 °C which is described in the first part. The XRD image for PtSe$_2$ in Fig. 6b is the magnification of that shown in Fig. 1, for which a PtSe$_2$ [001] peak can be clearly identified, along with the strong WSe$_2$ [001] peak shown in Fig. 6a (Sample III). On the other hand, the
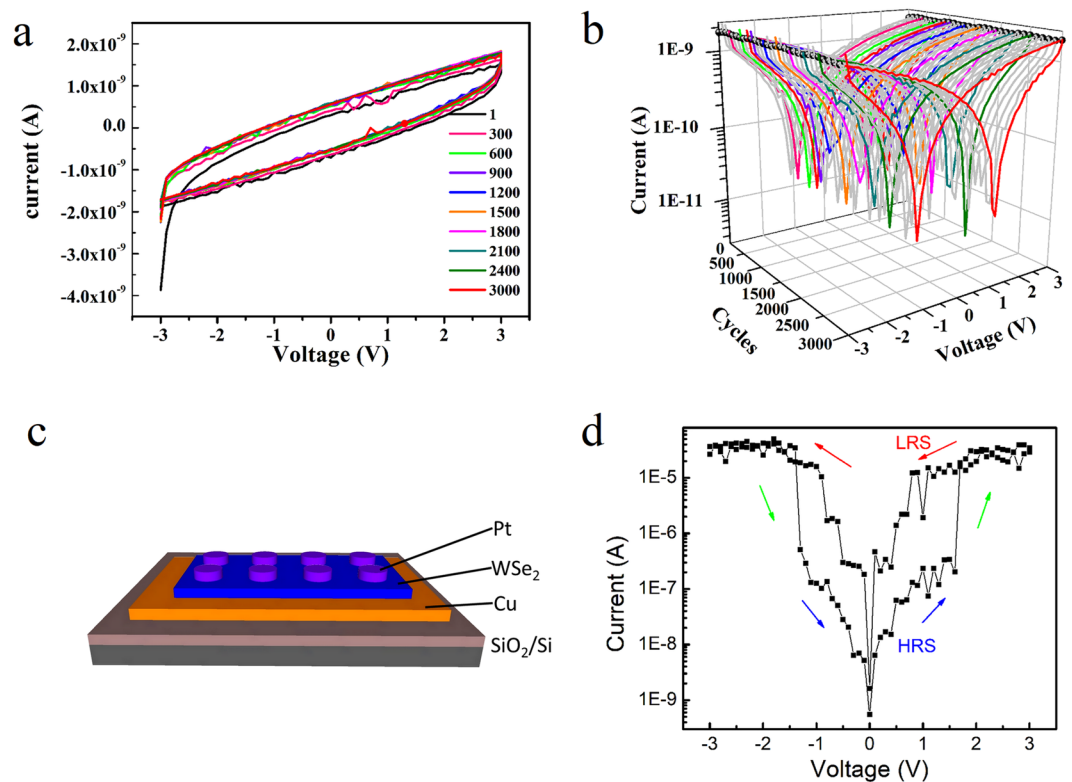
Figure 5. Device performance of two memory devices. (**a**) I-V curves for 3000 times of the as grown structure. Electrode size: 300 μm in dimension. (**b**) The I-V curves of (**a**) in semilogarithmic scale. Butterfly shaped curves are presented. (**c**) A ReRAM device structure composed of an exfoliated WSe$_2$ nanosheet, with Pt the top electrode, and Cu the bottom electrode. (**d**) I-V characteristic of the device shown in (**c**).
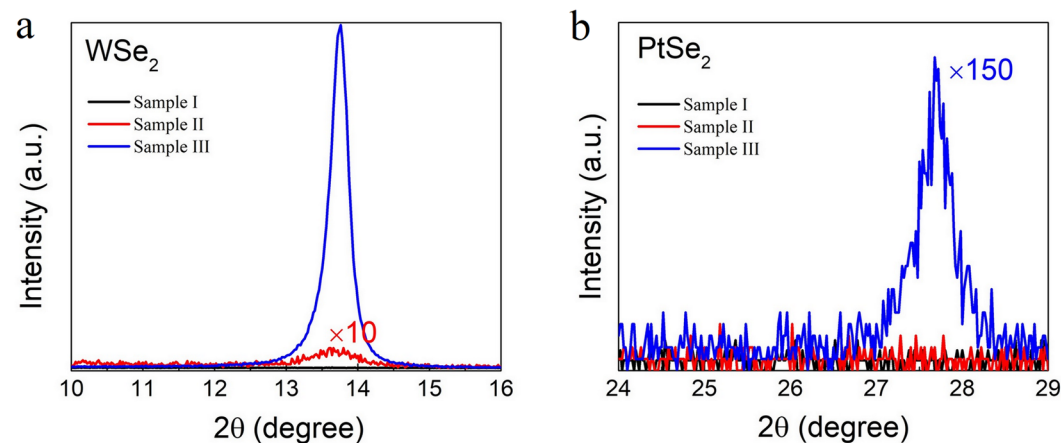

Figure 6. XRD patterns of the samples (I to III) grown at different conditions. (**a**) WSe$_2$. (**b**) PtSe$_2$. Sample I is grown at the selenization temperature of 350 °C. Sample II is firstly heated at 350 °C, and then increased to 450 °C. Sample III is firstly heated at 350 °C and then increased to 550 °C.

growth of WSe$_2$ directly on SiO$_2$/Si without a Pt underlayer reveals poor crystalline quality (Fig. S3a). These results imply that PtSe$_2$ could play an important role in promotion of the growth of WSe$_2$. To understand this, we have further conducted cross-sectional TEM studies to confirm the atomic structure of the stacked film structure. Figure 7a shows the TEM image close to the top interface. Interestingly, a highly ordered PtSe$_2$ buffer layer is found self-assembled below WSe$_2$, compared to the complicated disordered interlayer. The FFT pattern shows a hexagonal lattice structure for both WSe$_2$ and PtSe$_2$ along the [001] direction, with a d-spacing of 6.4 Å and 2.5 Å respectively, consistent with the report by Wang *et al.*[45]. To demonstrate the growth scheme, the atomic geometry of the composite system is shown in Fig. 7b,c. As reported, both WSe$_2$ and PtSe$_2$ have a hexagonal structure with lattice constants a = b = 0.328 nm for WSe$_2$ and a = b = 0.373 nm for PtSe$_2$ respectively[45,46]. Even with a similar
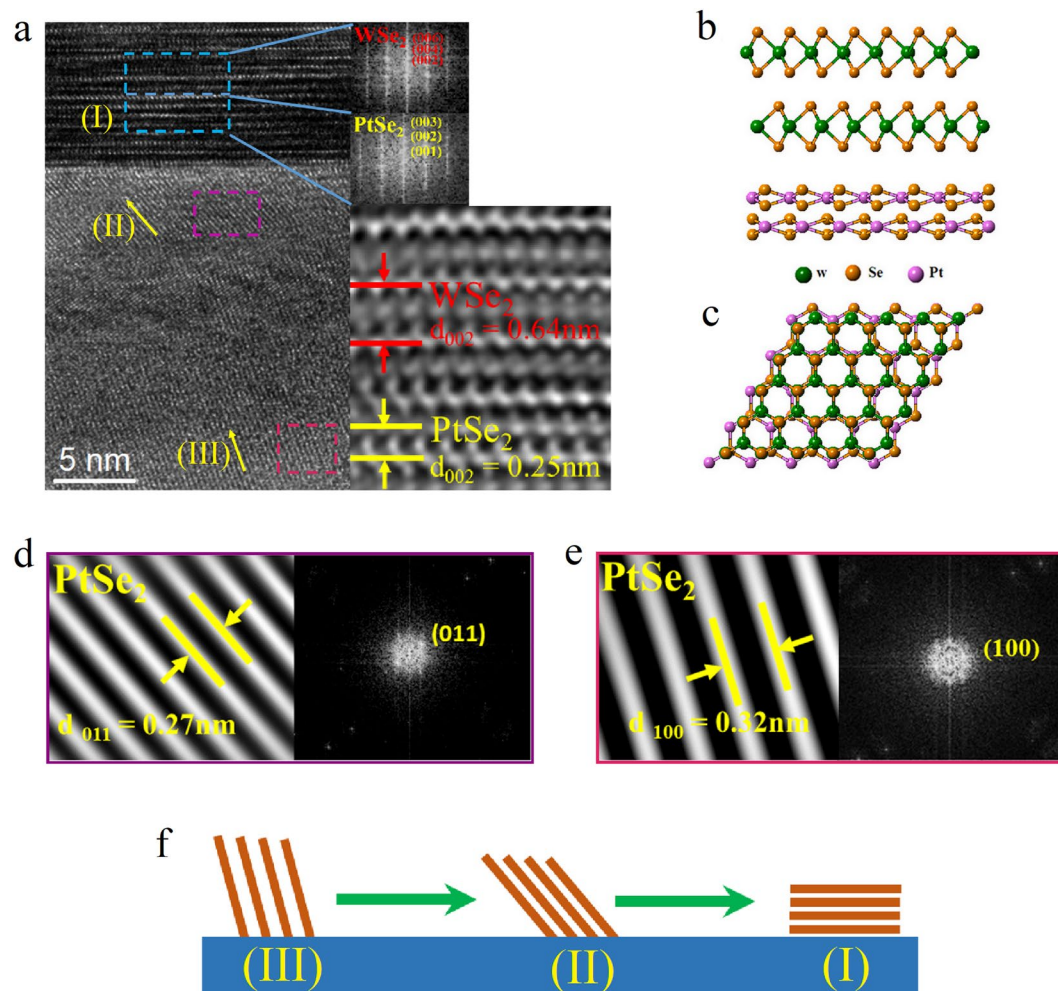
Figure 7. The growth of WSe$_2$ assisted by the formation of a PtSe$_2$ buffer layer. (**a**) Cross-sectional TEM image around the top interface. Right is a higher magnification of the cyan-color marked area, and the corresponding FFT patterns for the upper and lower regions, respectively. (**b,c**) Schematic illustration of the atomic structure of the WSe$_2$/PtSe$_2$ heterostructure: side-view and top view. The van der Waals epitaxial growth mode. (**d**) A higher magnification of the area near the top interface - the purple-color marked area in (**a**) (region II), and the corresponding FFT pattern. (**e**) The magnified image and the corresponding FFT pattern of the pink-color marked area in (**a**) (region III). (**f**) Schematic illustration of the growth process of PtSe$_2$.

hexagonal atomic structure, a large in-plane lattice mismatch of 12.1% exists between two (001) planes. The growth mode is attributed to the so-called van der Waals epitaxial growth[1,47], in contrast to the traditional epitaxial growth mode which requires a good lattice matching between two crystals. Epitaxial heterostructures by weak van der Waals interactions have been successfully realized for various 2D material systems in recent years[1–4].

The region below the highly epitaxial WSe$_2$/PtSe$_2$ layers is a highly disordered interlayer. To further investigate the role of this layer, a detailed TEM analysis is also performed. It shows that complex phases are formed in the interlayer. Figure 7d shows the magnified image for the marked area (purple, region II, Fig. 7a) close to the top interface, where the HRTEM image and the corresponding FFT pattern reveal a PtSe$_2$ lattice structure, with the (011) orientation. Compared to the above continuous PtSe$_2$ layers (lower cyan-color marked area), the PtSe$_2$ in the interlayer is more like a nano-crystalline structure surrounded by other phases. In the interlayer away from the interfaces, a highly disordered zone is formed, indicating complicated thermal diffusion dynamics during the growth process. Moreover, the crystalline PtSe$_2$ away from the top interface is also investigated. Figure 7e illustrates the magnified image of the pink-color marked area in Fig. 7a (region III), and a PtSe$_2$ lattice structure with the (100) orientation is shown. Different crystal orientations lead to different surface energies. In crystal growth, the mobile species tend to seek out low-energy positions and the equilibrium crystal states. The calculation of MoS$_2$ shows that (001) plane has a much lower surface energy than the other directions[48]. With a similar structure to MoS$_2$, it is reasonable to infer that the (001) plane for PtSe$_2$ also has the lowest surface energy. As expected from the growth kinetics, the preferred growth orientation follows the crystalline plane which has the lowest energy. The simplified thermodynamic model for PtSe$_2$ grown in the interlayer on the basis of the surface energy is shown in Fig. 7f, similar to the vertical to horizontal growth kinetics as reported[48]. Following the route to lower the energies, the highly ordered (001) PtSe$_2$ buffer layer with the lowest surface energy is formed on the top of

the disordered interlayer. The self-assembled (001) $PtSe_2$ buffer layer then promotes the formation of (001) WSe_2 epitaxial film through van der Waals epitaxial growth. Besides $PtSe_2$, Pt_2W has also been found at the interlayer region close to the bottom interface, for which we believe that the Pt-W alloy could come from the high temperature reaction process (see Supplementary Fig. S8 for more details). Through reducing the initial Pt thickness or increasing the selenization time, such alloy can be prevented (see Supplementary Figs S6 and S9 for details). Therefore, we believe that the presence of Pt_2W is not critical to the growth of WSe_2.

In parallel with the W 100 nm/Pt 100 nm sample, we also did cross-sectional HRTEM analysis of a thinner sample with the initial thicknesses of W 5 nm/Pt 2 nm. A $PtSe_2$ buffer layer has also been observed after selenization (see Supplementary Fig. S10 for more details). With help from the Pt underlayer, great advantages have been established, compared to the direct growth of WSe_2 on SiO_2/Si. The balance between surface energy and interface energy as well as the balance between energetics and kinetics, controls the growth process. The disordered interlayer region comes from complex reactions during the high temperature selenization process. Although the growth kinetics need to be further investigated for the interlayer region, we suggest that this interlayer between the highly epitaxial WSe_2/$PtSe_2$ layers and the substrate might behave as a buffer to accommodate the complicated balance, leading to the formation of the self-assembled $PtSe_2$, which finally promotes the epitaxial growth of WSe_2.

Large surface energy, poor wettability and the large lattice mismatch between a TMDC material and an insulating substrate are three common challenges in achieving high quality crystalline films[20]. Direct growth of large area WSe_2 as well as other TMDC materials on SiO_2/Si has been proved to be very difficult. The introduction of a buffer layer could be the choice to overcome such difficulties. Recently, growth of high quality graphene on SiO_2/Si with a boron nitride buffer layer has been reported[49]. Analogous to a buffer layer in conventional epitaxy[50], the mechanism and the method proposed here has a similar advantage, and could be applied to the growth of other TMDC materials.

Conclusion

In summary, we have reported an example of epitaxial growth of WSe_2 on inch-sized SiO_2/Si using a two-step selenization method. Crystalline WSe_2 thin films with high uniformity have been obtained, which shows great potential of this method for large-scale fabrications. The existence of the self-assembled $PtSe_2$ buffer layer promotes the (001) WSe_2 growth through the van der Waals epitaxial growth mode. Based on the fabricated thin films, high performance memory devices have also been demonstrated. Although the detailed underlying growth mechanisms need to be further explored, the method and the strategy described here may be applicable to the preparation of other TMDC materials in a large scale mode at a much lower temperature, and open up new possibilities in 2D materials engineering and applications.

Methods

Epitaxial WSe_2 growth. Substrates cut from silicon wafer with 300 nm thermally grown SiO_2 on top were used for the growth. Prior to the Pt film deposition, a 3 nm Ta was deposited as the adhesion layer, by magnetron sputtering. Then W with variable thicknesses was deposited by another sputtering process. α-W(110)/Pt(111) was achieved after the process. Then the α-W(110)/Pt(111)/Ta/SiO_2/Si substrate was placed at the center of a tubular furnace (4-inch-diameter tube). Selenium ingots (0.3 g) were placed in a separate ceramic boat, 6.5 cm away from the sample. The Se vapor was delivered by a N_2 flowing gas. The sample was first heated to 350 °C and annealed for 30 min, followed by the final treatment at 550 °C for about 12 seconds. Finally, the furnace was naturally cooled to room temperature.

Characterization. The crystallinity of the samples was determined by X-ray diffraction (XRD) using a diffractometer with Cu Kα radiation (Shimadzu LabX XRD-6000). Grazing-incidence XRD (GIXRD) measurements were performed with D8 Discover with GADDS (Bruker AXS Gmbh, Karisruhe, Germany). Cross-sectional transmission electron microscopy (TEM) images were taken with a FEI Tecnai Osiris system and top-view TEM images were taken with a FEI Tecnai F20 system. The morphologies of the prepared samples were obtained using a field emission scanning electron microscopy (SEM) (Hitachi, S-8010). X-ray photoemission spectroscopy (XPS) was performed by a Ulvac-PHI 1600 spectrometer with monochromatic Al Kα X-ray radiation (1486.6 eV). Raman and photoluminescence (PL) spectroscopy were conducted with HORIBA LabRAM HR800 except for the Raman mapping. We used 632 nm excitation wavelength for the measurements. The Si peak at 520 cm^{-1} was used as a reference for wavenumber calibration. The Raman mapping was performed on Nanofinder 30 (Tokyo Instruments, Inc.).

References

1. Geim, A. K. & Grigorieva, I. V. Van der Waals heterostructures. *Nature* **499**, 419–425 (2013).
2. Lin, Z. *et al.* 2D materials advances: from large scale synthesis and controlled heterostructures to improved characterization techniques, defects and applications. *2D Mater.* **3**, 042001 (2016).
3. Tan, C. *et al.* Recent advances in ultrathin two-dimensional nanomaterials. *Chem. Rev.* **117**, 6225–6331 (2017).
4. Novoselov, K., Mishchenko, A., Carvalho, A. & Neto, A. C. 2D materials and van der Waals heterostructures. *Science* **353**, aac9439 (2016).
5. Radisavljevic, B., Radenovic, A., Brivio, J., Giacometti, I. V. & Kis, A. Single-layer MoS$_2$ transistors. *Nat. Nanotechnol.* **6**, 147–150 (2011).
6. Wang, H. *et al.* Integrated circuits based on bilayer MoS$_2$ transistors. *Nano Lett.* **12**, 4674–4680 (2012).
7. Chuang, H.-J. *et al.* High mobility WSe$_2$ p-and n-type field-effect transistors contacted by highly doped graphene for low-resistance contacts. *Nano Lett.* **14**, 3594–3601 (2014).
8. Liu, W. *et al.* Role of metal contacts in designing high-performance monolayer n-type WSe$_2$ field effect transistors. *Nano Lett.* **13**, 1983–1990 (2013).
9. Ross, J. S. *et al.* Electrically tunable excitonic light-emitting diodes based on monolayer WSe$_2$ pn junctions. *Nat. Nanotechnol.* **9**, 268–272 (2014).

10. Yang, W. *et al*. Electrically tunable valley-light emitting diode (vLED) based on CVD-grown monolayer WS2. *Nano Lett.* **16**, 1560–1567 (2016).
11. Zhou, N. *et al*. P-GaSe/N-MoS$_2$ Vertical heterostructures synthesized by van der Waals epitaxy for photoresponse modulation. *Small* **14**, 1702731 (2018).
12. Wang, Z. *et al*. Giant photoluminescence enhancement in tungsten-diselenide–gold plasmonic hybrid structures. *Nat. Commun.* **7**, 11283 (2016).
13. Acerce, M., Voiry, D. & Chhowalla, M. Metallic 1T phase MoS$_2$ nanosheets as supercapacitor electrode materials. *Nat. Nanotechnol.* **10**, 313 (2015).
14. Deng, S. *et al*. Directional construction of vertical nitrogen doped 1T 2H MoSe$_2$/graphene shell/core nanoflake arrays for efficient hydrogen evolution eeaction. *Adv. Mater.* **29**, 1700748 (2017).
15. Boscher, N. D., Carmalt, C. J. & Parkin, I. P. Atmospheric pressure chemical vapor deposition of WSe$_2$ thin films on glass—highly hydrophobic sticky surfaces. *J. Mater. Chem.* **16**, 122–127 (2006).
16. Huang, J.-K. *et al*. Large-area synthesis of highly crystalline WSe$_2$ monolayers and device applications. *ACS Nano* **8**, 923–930 (2013).
17. Liu, B. *et al*. Chemical vapor deposition growth of monolayer WSe$_2$ with tunable device characteristics and growth mechanism study. *ACS Nano* **9**, 6119–6127 (2015).
18. Chen, J. *et al*. Chemical vapor deposition of large sized hexagonal WSe$_2$ crystals on dielectric substrates. *Adv. Mater.* **27**, 6722–6727 (2015).
19. Liu, J. *et al*. Ultrafast self-limited growth of strictly monolayer WSe$_2$ crystals. *Small* **12**, 5741–5749 (2016).
20. Li, H., Li, Y., Aljarb, A., Shi, Y. & Li, L.-J. Epitaxial growth of two-dimensional layered transition-metal dichalcogenides: growth mechanism, controllability, and scalability. *Chem. Rev.* **118**, 6134–6150 (2017).
21. Li, H. *et al*. Texture control and growth mechanism of WSe$_2$ film prepared by rapid selenization of W film. *Appl. Surf. Sci.* **394**, 142–148 (2017).
22. Nguyen, N. T. *et al*. Synthesis and properties of turbostratically disordered, ultrathin WSe$_2$ films. *Chem. Mater.* **22**, 2750–2756 (2010).
23. Gremenok, V. *et al*. Preparation of Cu(In,Ga)Se$_2$ thin film solar cells by two-stage selenization processes using N$_2$ gas. *Sol. Energy Mater. Sol. Cells* **89**, 129–137 (2005).
24. Cai, C.-H. *et al*. Interplay between potassium doping and bandgap profiling in selenized Cu(In,Ga)Se$_2$ solar cells: A functional CuGa: KF surface precursor layer. *Nano Energy* **47**, 393–400 (2018).
25. Emori, S. & Beach, G. S. Optimization of out-of-plane magnetized Co/Pt multilayers with resistive buffer layers. *J. Appl. Phys.* **110**, 033919 (2011).
26. Yin, Y. *et al*. Significantly increased Raman enhancement on MoX$_2$ (X = S, Se) monolayers upon phase transition. *Adv. Funct. Mater.* **27**, 1606694 (2017).
27. Maitra, U. *et al*. Highly effective visible-light-induced H2 generation by single-layer 1T-MoS$_2$ and a nanocomposite of few-layer 2H-MoS$_2$ with heavily nitrogenated graphene. *Angew. Chem.* **125**, 13295–13299 (2013).
28. Eda, G. *et al*. Coherent atomic and electronic heterostructures of single-layer MoS$_2$. *ACS Nano* **6**, 7311–7317 (2012).
29. Ambrosi, A., Sofer, Z. & Pumera, M. 2H → 1T phase transition and hydrogen evolution activity of MoS$_2$, MoSe$_2$, WS$_2$ and WSe$_2$ strongly depends on the MX2 composition. *Chem. Commun.* **51**, 8450–8453 (2015).
30. Su, S. *et al*. Uniform Au@ Pt core–shell nanodendrites supported on molybdenum disulfide nanosheets for the methanol oxidation reaction. *Nanoscale* **8**, 602–608 (2016).
31. Del Corro, E. *et al*. Excited excitonic states in 1L, 2L, 3L, and bulk WSe$_2$ observed by resonant Raman spectroscopy. *ACS Nano* **8**, 9629–9635 (2014).
32. Zhao, W. *et al*. Lattice dynamics in mono- and few-layer sheets of WS$_2$ and WSe$_2$. *Nanoscale* **5**, 9677–9683 (2013).
33. Kruskopf, M. *et al*. Comeback of epitaxial graphene for electronics: large-area growth of bilayer-free graphene on SiC. *2D Mater.* **3**, 041002 (2016).
34. Medina, H. *et al*. Wafer-scale growth of WSe$_2$ monolayers toward phase-engineered hybrid WOx/WSe$_2$ films with sub-ppb NOx gas sensing by a low-temperature plasma-assisted selenization process. *Chem. Mater.* **29**, 1587–1598 (2017).
35. Novoselov, K. S. *et al*. Electric field effect in atomically thin carbon films. *Science* **306**, 666–669 (2004).
36. Hernandez, Y. *et al*. High-yield production of graphene by liquid-phase exfoliation of graphite. *Nat. Nanotechnol.* **3**, 563–568 (2008).
37. Huang, Y. *et al*. Reliable exfoliation of large-area high-quality flakes of graphene and other two-dimensional materials. *ACS Nano* **9**, 10612–10620 (2015).
38. Fan, X. *et al*. Controlled exfoliation of MoS$_2$ crystals into trilayer nanosheets. *J. Am. Chem. Soc* **138**, 5143–5149 (2016).
39. Lin, Y.-C. *et al*. Wafer-scale MoS$_2$ thin layers prepared by MoO$_3$ sulfurization. *Nanoscale* **4**, 6637–6641 (2012).
40. Luo, X. *et al*. Effects of lower symmetry and dimensionality on Raman spectra in two-dimensional WSe$_2$. *Phys. Rev. B* **88**, 195313 (2013).
41. Paul, S., Kanwal, A. & Chhowalla, M. Memory effect in thin films of insulating polymer and C$_{60}$ nanocomposites. *Nanotechnology* **17**, 145 (2005).
42. Cook, J. B. *et al*. Pseudocapacitive charge storage in thick composite MoS$_2$ nanocrystal based electrodes. *Adv. Energy Mater.* **7**, 1601283 (2017).
43. Fowler, B. W. *et al*. Electroforming and resistive switching in silicon dioxide resistive memory devices. *RSC Adv.* **5**, 21215–21236 (2015).
44. Du, Y. *et al*. Symmetrical negative differential resistance behavior of a resistive switching device. *ACS Nano* **6**, 2517–2523 (2012).
45. Wang, Y. *et al*. Monolayer PtSe$_2$, a new semiconducting transition-metal-dichalcogenide, epitaxially grown by direct selenization of Pt. *Nano Lett.* **15**, 4013–4018 (2015).
46. Salitra, G., Hodes, G., Klein, E. & Tenne, R. Highly oriented WSe$_2$ thin films prepared by selenization of evaporated WO$_3$. *Thin Solid Films* **245**, 180–185 (1994).
47. Koma, A. V. der Waals epitaxy - a new epitaxial growth method for a highly lattice-mismatched system. *Thin Solid Films* **216**, 72–76 (1992).
48. Fei, L. *et al*. Direct TEM observations of growth mechanisms of two-dimensional MoS$_2$ flakes. *Nat. Commun.* **7**, 12206 (2016).
49. Entani, S., Takizawa, M., Li, S., Naramoto, H. & Sakai, S. Growth of graphene on SiO$_2$ with hexagonal boron nitride buffer layer. *Appl. Surf. Sci.* **475**, 6–11 (2019).
50. Utama, M. I. B. *et al*. Recent developments and future directions in the growth of nanostructures by van der Waals epitaxy. *Nanoscale* **5**, 3570–3588 (2013).

Acknowledgements

Author Contributions

P.C.W., C.L.Y. and Y.D. performed experiments and data analysis. Y.D., P.C.W. and C.H.L. wrote the manuscript. Y.D. and C.H.L. proposed the mechanism. C.H.L. supervised the project. All authors commented on the manuscript.

Additional Information

Supplementary information accompanies this paper at https://doi.org/10.1038/s41598-019-44518-3.

Competing Interests: The authors declare no competing interests.

Publisher's note: Springer Nature remains neutral with regard to jurisdictional claims in published maps and institutional affiliations.